Entanglement Distillation between Solid-State Quantum Network Nodes

N. Kalb[1,2,*], A. A. Reiserer[1,2,*,‡], P. C. Humphreys[1,2,*], J. J. W. Bakermans[1,2], S. J. Kamerling[1,2], N. H. Nickerson[3], S. C. Benjamin[4], D. J. Twitchen[5], M. Markham[5], R. Hanson[1,2,†]

[1]QuTech, Delft University of Technology, P. O. Box 5046, 2600 GA Delft, The Netherlands
[2]Kavli Institute of Nanoscience, Delft University of Technology, P. O. Box 5046, 2600 GA Delft, The Netherlands
[3]Department of Physics, Imperial College London, Prince Consort Road, London SW7 2AZ, U.K.
[4]Department of Materials, University of Oxford, Parks Road, Oxford OX1 3PH, U.K.
[5]Element Six Innovation, Fermi Avenue, Harwell Oxford, Didcot, Oxfordshire OX11 0QE, U.K.
[*] These authors contributed equally to this work.
[†]To whom correspondence should be addressed; E-mail: r.hanson@tudelft.nl.
[‡]Present address: Quantum Networks Group, Max-Planck-Institute of Quantum Optics, Hans-Kopfermann-Str. 1, 85748 Garching, Germany

One Sentence Summary:

Entanglement distillation is demonstrated on a universal quantum network backbone of remote solid-state two-qubit nodes.

Abstract:

The impact of future quantum networks hinges on high-quality quantum entanglement shared between network nodes. Unavoidable imperfections necessitate means to improve remote entanglement by local quantum operations.

We realize entanglement distillation on a quantum network primitive of distant electron-nuclear two-qubit nodes. The heralded generation of two copies of a remote entangled state is demonstrated through single-photon-mediated entangling of the electrons and robust storage in the nuclear spins. After applying local two-qubit gates, single-shot measurements herald the distillation of an entangled state with increased fidelity that is available for further use. The key combination of generating, storing and processing entangled states should enable the exploration of multi-particle entanglement on an extended quantum network.

Future quantum networks connecting nodes of long-lived stationary qubits through photonic channels may enable secure communication, quantum computation and simulation, and enhanced metrology (*1–9*). The power of these applications fundamentally derives from quantum entanglement shared between the network nodes. The key experimental challenge is therefore to establish high-quality remote entanglement in the presence of unavoidable errors such as decoherence, photon loss and imperfect quantum control. Remarkably, by only using classical communication and local quantum operations, a high-fidelity remote entangled state can be distilled from several lower-fidelity copies (*10, 11*) (Fig. 1A). Success of this intrinsically probabilistic distillation can be non-destructively heralded by measurement outcomes such that the distilled state is available for further use, a critical requirement for scalable networks. Owing to these unique features, entanglement distillation (or purification) has become a central building block of quantum network proposals (*6–9, 12, 13*).

Generation and distillation of remote entangled states. To run entanglement distillation on a quantum network, several copies of a raw entangled state must first be shared between the nodes. This can be achieved using a network primitive of two nodes with two qubits each: a

communication qubit with an optical interface for generating remote entanglement and a memory qubit for storage (Fig. 1B). First the communication qubits run the entangling protocol, which due to photon loss is intrinsically probabilistic. After photon detection heralds the generation of a raw entangled state on the communication qubits, this state is swapped onto the memory qubits. The communication qubits are then used to generate a second raw entangled state. At this point, the network nodes share two nominally identical copies of the raw state, from which an entangled state of higher fidelity can be distilled. This protocol thus exploits the combination of heralded generation of remote entanglement with robust quantum state storage, high-fidelity quantum logic gates and non-demolition qubit readout within each node.

These demanding experimental requirements have so far limited the exploration of distillation on entangled qubits to four ions within a single node (*14*) and to all-photonic protocols without memories in which the distilled state was unavoidably lost upon success (*15–17*). As an important step towards the desired quantum network, heralded entanglement between distant stationary qubits has recently been achieved with ions, atoms, nitrogen-vacancy (NV) defect centers, quantum dots and superconducting qubits (*18–23*). However, the potential memory qubits investigated so far in conjunction with these protocols (*24, 25*) suffered from rapid dephasing during remote entangling attempts due to unwanted couplings, thus precluding the generation of multiple remote entangled states as required for distillation.

We realize the distillation of entangled states on an elementary quantum network consisting of a pair of two-qubit solid-state nodes separated by two meters (Fig. 1B). We implement a single-photon-based entangling protocol using diamond electron-spin qubits (communication qubits) while capitalizing on recent progress on quantum control (*26*) and robust state storage (*27*) in nuclear-spin-based quantum memories. Real-time feedback is implemented to compensate memory qubit phase-shifts induced by the probabilistic nature of the remote entangling protocol. As an immediate advantage, the demonstrated protocol distinctly increases the effi-

ciency of entanglement generation compared to the standard two-photon-coincidence protocols used in earlier works (*25, 28*), while removing the optical path-length dependence of stand-alone probabilistic single-photon protocols (*22, 29*).

Quantum network nodes. Our quantum network nodes comprise an NV electron spin in diamond as a communication qubit and a nearby carbon-13 nuclear spin as a memory qubit. The diamond chips holding these qubits reside in individual closed-cycle cryostats ($T = 4\,\mathrm{K}$) that are separated by two meters (*30*). The electron spin state is manipulated using amplitude-shaped microwave pulses. Electron spin decoherence occurs on timescales exceeding a millisecond and has negligible impact on the presented results. Spin-selective resonant optical excitation enables high-fidelity initialization and single-shot non-demolition read-out of the electron spin (*31*), as well as generation of spin-photon entanglement for connecting distant nodes (*20*) (see also Fig. S4). We use nuclear spins with intrinsic dephasing times T_2^* of $3.4(1)$ ms and $16.2(3)$ ms for node A and B, respectively (*30*). We implement universal control on each of these nuclear spin qubits by exploiting its hyperfine coupling to the electron spin through recently developed dynamical-decoupling-based gate sequences (*32*). This complete quantum toolbox enables the implementation of all four steps in the distillation protocol.

Fig. 1C shows the compilation of the full gate circuit into the quantum control operations of our platform. This compilation maximizes the repetition rate and minimizes the number of local quantum gates following the generation of the first remote state. In particular, by initializing the memory qubit at the start of the protocol we are able to implement the SWAP operation with just two conditional quantum gates instead of the three that would be required for arbitrary input states (*30*). Note that our SWAP implementation maps the communication qubit energy eigenstates onto memory superposition states $|\pm X\rangle \equiv (|0\rangle \pm |1\rangle)/\sqrt{2}$.

To benchmark the performance of the local quantum logic we execute a combination of the

SWAP (yellow box in Fig. 1C) and the gates of the distillation step (purple box in Fig. 1C) to generate a maximally-entangled Bell-state between the communication and memory qubits (see Fig. 2A). The full density matrix of the resulting two-qubit state is reconstructed via quantum state tomography (QST, see ref. (*30*) for further details). We find a fidelity with the ideal Bell state of $0.96(1)$ ($0.98(1)$) for node A (B) indicating high-quality operations in both nodes (Fig. 2B).

Robust storage of quantum information. A critical capability for the network nodes is the robust storage of quantum information in the memories while the communication qubits are used to generate remote entangled states. This requires the memory qubits to have long coherence times and be resilient to operations on the communication qubit. The generation of remote entanglement, in particular, poses two challenges as its probabilistic nature means that an a priori unknown number of attempts is required.

First, each failed entangling attempt leaves the communication qubits in an unknown state which necessitates a reset by optical pumping. This reset is a stochastic process which, in combination with the always-on hyperfine interaction between communication and memory qubit, causes dephasing of stored memory states (*27, 33*). Memories with a small parallel hyperfine coupling are used so that the precession frequency of these memories exhibits only a weak dependency $\Delta\omega$ on the state of the communication qubit during the repumping process of a few hundred nanoseconds ($\Delta\omega_{\mathrm{A}} = 2\pi \cdot 22.4(1)\,\mathrm{kHz}$ and $\Delta\omega_{\mathrm{B}} = 2\pi \cdot 26.6(1)\,\mathrm{kHz}$). Decoherence via the perpendicular hyperfine component is suppressed by an applied magnetic field of about $40\,\mathrm{mT}$.

Second, the interaction between communication and memory qubit leads to a deterministic phase-shift $\varphi_{A/B}$ on the memory per entangling attempt. Because it is unknown which entangling attempt will herald success, real-time feedback on the memory is required to compensate

for these phase-shifts before the final two-qubit gate of Fig. 1C is applied. In addition, the feedback must preserve the coherence of the communication qubit as it holds the second copy of the raw entangled state. We realize such real-time feedback through dynamical decoupling of the electron spin synced with the nuclear spin precession frequency that induces an electron-state-independent phase gate on the memory (*32*). At each node, the number of entangling attempts until success N is tracked by a microprocessor that terminates the subsequent decoupling sequence when the desired rotation $\mathrm{R_z}(\varphi_{A/B})^N$ has been applied. Ideally, this leaves the memory with the desired phase relation regardless of the number of entangling attempts. We calibrate and verify this feedback at each node separately (see Fig. 3A and Fig. 3B) and measure a negligible effect on the memory state fidelity while the state of the communication qubit is preserved as desired.

With this feedback realized, we investigate the robustness of the memory as a function of the elapsed entangling attempts. The memory is initialized in one of the six cardinal states of the Bloch sphere ($|0\rangle$,$|1\rangle$,$|\pm\mathrm{X}\rangle$ and $|\pm\mathrm{Y}\rangle \equiv (|0\rangle \pm i|1\rangle)/\sqrt{2}$), execute a number of entangling attempts followed by phase-feedback and measure the relevant memory expectation value (see Fig. 3C). Dephasing-sensitive states $|\pm\mathrm{X}\rangle, |\pm\mathrm{Y}\rangle$ decay with $1/e$-values of $273(5)$ ($272(4)$) entangling attempts in node A (node B) whereas the energy eigenstates $|0\rangle, |1\rangle$ are preserved with high fidelity as expected. The memories thus provide faithful storage during remote entangling attempts.

Experimental entanglement distillation. With local control and storage in place, we now turn towards the execution of the full distillation protocol (Figs. S1 and S2). Following Ref. (*34*), we generate the remote states that provide the resources for distillation by first initializing both communication qubits in a superposition with variable angle θ, $|\theta\rangle \equiv \sin\theta|0\rangle - i\cos\theta|1\rangle$. Subsequent optical excitation for state $|0\rangle$ and overlap of the emission of both communication

qubits on a beam splitter (see steps 1 and 3 of Fig. 1C and histograms in Fig. S3) generates the raw remote state ρ_{raw} if a single photon is detected (*34*). For equal and small detection probabilities for both nodes and negligible dark counts, ρ_{raw} reads:

$$\rho_{\mathrm{raw}} = \left(1 - \sin^2\theta\right) |\Psi_\phi^\pm\rangle\langle\Psi_\phi^\pm| + \sin^2\theta\, |0,0\rangle\langle 0,0|. \tag{1}$$

The states $|\Psi_\phi^\pm\rangle \equiv (|01\rangle \pm e^{i\phi}|10\rangle)/\sqrt{2}$ are entangled states, with a relative phase depending on which detector clicked ($\pm$) and an additional internal phase ϕ due to the unknown path length between both emitters and the beam splitter. The fraction of the non-entangled admixture $|0,0\rangle\langle 0,0|$ can be directly controlled through the choice of the initial communication qubit state $|\theta\rangle$; note that the choice of $|\theta\rangle$ also affects the probability of successful entanglement generation (scaling as $\sin^2\theta$). We next swap the raw state onto the memories such that the communication qubit is free for another round of remote state generation (step 2 in Fig. 1C). Once a second state is successfully generated (step 3), we apply a conditional quantum gate within each node and read out the communication qubits in a single shot. Owing to the quantum non-demolition nature of this readout the memory qubits do not experience additional dephasing during this step (*31*). Readout of the communication qubit projects the memories into one of four states depending on the readout results (*30*):

$$\begin{aligned}
(0_A, 0_B) &: \tfrac{1}{2}\cos^4\theta\, U|\Psi_0^\pm\rangle\langle\Psi_0^\pm|U^\dagger, \\
(0_A, 1_B) &: \tfrac{1}{2}\sin^2\theta\cos^2\theta\, U(|0,1\rangle\langle 0,1| + |1,1\rangle\langle 1,1|)U^\dagger, \\
(1_A, 0_B) &: \tfrac{1}{2}\sin^2\theta\cos^2\theta\, U(|1,0\rangle\langle 1,0| + |1,1\rangle\langle 1,1|)U^\dagger, \\
(1_A, 1_B) &: \sin^4\theta\, U|1,1\rangle\langle 1,1|U^\dagger + \tfrac{1}{2}\cos^4\theta\, U|\Psi_{2\phi}^\pm\rangle\langle\Psi_{2\phi}^\pm|U^\dagger.
\end{aligned}$$

Here the states are left unnormalized; their traces indicate their probabilities of occurrence. The unitary U corresponds to a Hadamard gate on each memory that arises from the swapping operation in each node. Observation of the readout combination (0_A,0_B) heralds successful

distillation and leaves the system in the state

$$|\psi\rangle_{\mathrm{c}} \otimes |\psi\rangle_{\mathrm{m}} = e^{i\phi}|0,0\rangle \otimes U|\Psi_0^{\pm}\rangle \tag{2}$$

with the relative phase of the final Bell state given by the photon detection signature, i.e. the photons in step 1 and 3 were detected in the same (+) or in different (-) output ports. Importantly, the protocol is agnostic to correlated dephasing of the raw states and is therefore only sensitive to optical path length drifts that occur within an individual run of the protocol (see Fig. S7) (*34*). This is in stark contrast to probabilistic single-photon protocols (*22, 23, 29, 35*) that require path length stabilization over the full course of data acquisition.

The experimental implementation of entanglement generation requires that the communication qubits' optical transitions are kept on resonance despite shot-to-shot fluctuations and long-term drifts of the respective local charge environments. An automatic feedback loop and resonance search routine is used to compensate for charge jumps such that the experiment is push-button and runs without human intervention. To further optimize the data rate the number of remote entangling attempts is bounded to 1000 for step 1 and up to 500 rounds for step 3, leading to event rates (i.e. two remote states were successfully generated) of around 10 Hz. These bounds are a compromise between maximizing the success probability (favoring more attempts) and minimizing effects of drifts and of memory decoherence (favoring fewer attempts).

Distillation results. We start by running the complete protocol using $\theta = \pi/6$ and perform full quantum state tomography on the distilled state. This way, using the complete information obtained on the resulting output, we can verify whether the protocol works as desired. Fig. 4A shows the resulting data for a maximum of 50 entangling attempts in the second round of state generation. This truncation yields optimal state storage during each run of the protocol (*30*). Quantitatively, the measured fidelity with the ideal Bell state of $0.65(3) > 0.5$ proves entanglement of the distilled state. Furthermore, the density matrix has high populations in

the Bell-state-subspace only, showing that the distillation successfully diminishes the separable admixture.

To gain further insight into the performance of the protocol we measure the fidelity of the distilled state for different amounts of the separable admixture in the raw states; i.e. for different θ (see Fig. 4B, blue dots). The results are again truncated after a maximum of 50 entangling attempts in the second round. The state fidelities are averaged over both detection signatures.

The hallmark of successful distillation is an increase in fidelity of the distilled state compared to that of the raw states. Whereas in the textbook description both raw states are assumed to be equal, in our experiment they are different due to imperfections in the swap operation and memory storage that only affect the raw state held by the memories, and path length variations on short timescales that only affect the raw state held by the communication qubits. To make a meaningful comparison we therefore consider the state fidelities of each of these raw states separately.

Because of the unreferenced internal phase of the raw states, all coherences are washed out due to optical path length variations. Direct tomography will therefore yield state fidelities that cannot surpass 0.5. As a result, the measured fidelities of the distilled states far exceed the electron state fidelities measured after step 1 (Fig. 4B, orange dots). Although these numbers reflect the current experiment, we now turn to a more strict comparison by taking into account that the internal phase may become accessible in future experiments through optical path stabilization.

We model the raw state fidelities at the start of the distillation step (step 4) using independently determined parameters under the assumption of a perfectly known initial path length difference (Fig. 4B, solid purple line for raw state on the electrons and solid orange line for raw state on the nuclei) (*30*). For small values of θ (small separable admixtures) the fidelity increase due to distillation is offset by the errors introduced with the additional quantum operations of the distillation step. However, we find that for larger values of θ the distilled state fidelity sig-

nificantly surpasses both of the raw state fidelities (see also Fig. S10 and (*30*) for hypothesis test). This result demonstrates the realization of entanglement distillation on our elementary quantum network.

For a more detailed understanding of the different error sources contributing to the measured fidelity, we develop an extensive model of the full protocol using independently measured quantities and two free parameters: one factor accounting for additional memory control errors and the second for phase fluctuations of the raw states (*30*). We find good agreement between the modeled fidelity and the data for each of the different separable admixtures (see Fig. 4B blue dashed line and (*30*)) and for the evolution of the correlations with number of entangling attempts (Fig. 4C). The model indicates that the state fidelities are mainly limited by memory qubit dephasing and control errors as well as non-zero two-photon distinguishability. The latter effect, quantified by a measured two-photon interference visibility of 0.73(3) (see Fig. S6), is especially harmful in the above comparison with the raw state, as this occurs twice for the distillation protocol but only once for the raw state generation. A visibility of 0.9 as observed on different NV center pairs (*28*) would thus yield an even stronger entanglement enhancement.

Ebit rate. Previously demonstrated entangling protocols based on two-photon coincidences (*25, 28*) require steps 1 and 3 to succeed in subsequent attempts leading to a success probability scaling with the square of the photon detection probability p_{det}. In contrast, the distillation protocol allows step 3 to succeed in one of many attempts following success in step 1, leading to a success probability scaling linearly with p_{det} in the ideal case. Given that in a typical quantum network setting p_{det} will be small (in our case $p_{\mathrm{det}} \approx 10^{-3}$), the distillation protocol can provide a distinct rate advantage despite the overhead of the additional local quantum logic.

To quantitatively compare our results with two-photon-coincidence protocols we upper bound the rate r of entangled bit (ebit) generation for each protocol using $r = \nu E_N$ with

the logarithmic negativity E_N and the rate of success ν. Fig. 5 compares the ebit rate of the presented distillation protocol to the modeled rate of the Barrett-Kok two-photon-coincidence protocol (*36*) used in earlier experiments on NV centers (*20, 28*). We find that the distillation protocol (blue dots) outperforms the two-photon-coincidence protocol for identical experimental conditions, not only when assuming the measured two-photon indistinguishability (orange solid line) but even for the case that the two-photon-coincidence protocol would be able to access perfect two-photon indistinguishability (orange dashed line).

Conclusion and outlook. The combination of generating, storing and processing remote entangled qubits as demonstrated in the current distillation experiment provides a universal primitive for realizing extended quantum networks. The distillation itself is a powerful method to counteract unavoidable decoherence as entanglement is distributed throughout the network. Also, the protocol enables a speedup of entanglement generation that can be harnessed in related platforms such as other solid-state defect centers (*37*) and trapped ions (*38*). Improvements can be expected by encoding qubits into decoherence-protected subspaces (*27*), by using isotopically purified materials with longer qubit dephasing times (*39–41*), by implementing a faster reset or a measurement-based reset of the communication qubit and by increasing the entangling rates through photonic cavities (*42, 43*). Furthermore, the techniques used in recent demonstrations of multi-qubit control and quantum error correction on a 4-qubit node (*26, 44*) are fully compatible with the current experiment, thus highlighting the potential for scaling to more qubits and extending network functionality in the near future. Finally, the methods developed provide the toolkit to explore and utilize many-particle entanglement on a multi-node quantum network.

References and Notes:

1. H. J. Kimble, *Nature* **453**, 1023 (2008).

2. M. Ben-Or, C. Crepeau, D. Gottesman, A. Hassidim, A. Smith, *47th Annual IEEE Symposium on Foundations of Computer Science* (2006).

3. A. Broadbent, J. Fitzsimons, E. Kashefi, *50th Annual IEEE Symposium on Foundations of Computer Science* (2009).

4. L. Jiang, *et al.*, *Phys. Rev. A* **79**, 032325 (2009).

5. A. Ekert, R. Renner, *Nature* **507**, 443 (2014).

6. J. I. Cirac, A. K. Ekert, S. F. Huelga, C. Macchiavello, *Phys. Rev. A* **59**, 4249 (1999).

7. D. Gottesman, T. Jennewein, S. Croke, *Phys. Rev. Lett.* **109**, 070503 (2012).

8. N. H. Nickerson, J. F. Fitzsimons, S. C. Benjamin, *Phys. Rev. X* **4**, 041041 (2014).

9. P. Kómár, *et al.*, *Nat. Phys.* **10**, 582 (2014).

10. C. H. Bennett, *et al.*, *Phys. Rev. Lett.* **76**, 722 (1996).

11. D. Deutsch, *et al.*, *Phys. Rev. Lett.* **77**, 2818 (1996).

12. W. Dür, H.-J. Briegel, J. I. Cirac, P. Zoller, *Phys. Rev. A* **59**, 169 (1999).

13. L. Childress, J. M. Taylor, A. S. Sørensen, M. D. Lukin, *Phys. Rev. Lett.* **96**, 070504 (2006).

14. R. Reichle, *et al.*, *Nature* **443**, 838 (2006).

15. J.-W. Pan, S. Gasparoni, R. Ursin, G. Weihs, A. Zeilinger, *Nature* **423**, 417 (2003).

16. P. G. Kwiat, S. Barraza-Lopez, A. Stefanov, N. Gisin, *Nature* **409**, 1014 (2001).

17. J.-W. Pan, *et al.*, *Rev. Mod. Phys.* **84**, 777 (2012).

18. D. L. Moehring, *et al.*, *Nature* **449**, 68 (2007).

19. J. Hofmann, *et al.*, *Science* **337**, 72 (2012).

20. H. Bernien, *et al.*, *Nature* **497**, 86 (2013).

21. A. Narla, *et al.*, *Phys. Rev. X* **6**, 031036 (2016).

22. A. Delteil, *et al.*, *Nat. Phys.* **12**, 218 (2016).

23. R. Stockill, *et al.*, *arXiv:1702.03422* (2017).

24. W. Pfaff, *et al.*, *Science* **345**, 532 (2014).

25. D. Hucul, *et al.*, *Nat. Phys.* **11**, 37 (2015).

26. J. Cramer, *et al.*, *Nat. Commun.* **7**, 11526 (2016).

27. A. Reiserer, *et al.*, *Phys. Rev. X* **6**, 021040 (2016).

28. B. Hensen, *et al.*, *Nature* **526**, 682 (2015).

29. L. Slodička, *et al.*, *Phys. Rev. Lett.* **110**, 083603 (2013).

30. Materials and methods are available as supplementary materials at the Science website.

31. M. S. Blok, *et al.*, *Nat. Phys.* **10**, 189 (2014).

32. T. H. Taminiau, J. Cramer, T. v. d. Sar, V. V. Dobrovitski, R. Hanson, *Nat. Nano.* **9**, 171 (2014).

33. L. Jiang, *et al.*, *Phys. Rev. Lett.* **100**, 073001 (2008).

34. E. T. Campbell, S. C. Benjamin, *Phys. Rev. Lett.* **101**, 130502 (2008).

35. C. Cabrillo, J. I. Cirac, P. García-Fernández, P. Zoller, *Phys. Rev. A* **59**, 1025 (1999).

36. S. D. Barrett, P. Kok, *Phys. Rev. A* **71**, 060310 (2005).

37. D. J. Christle, *et al.*, *Nat. Mater.* **14**, 160 (2015).

38. C. Monroe, J. Kim, *Science* **339**, 1164 (2013).

39. G. Balasubramanian, *et al.*, *Nat. Mater.* **8**, 383 (2009).

40. P. C. Maurer, *et al.*, *Science* **336**, 1283 (2012).

41. A. M. Tyryshkin, *et al.*, *Nat. Mater.* **11**, 143 (2012).

42. A. Faraon, P. E. Barclay, C. Santori, K.-M. C. Fu, R. G. Beausoleil, *Nat. Photon.* **5**, 301 (2011).

43. A. Sipahigil, *et al.*, *Science* **354**, 847 (2016).

44. N. Kalb, *et al.*, *Nat. Commun.* **7**, 13111 (2016).

45. L. Robledo, *et al.*, *Nature* **477**, 574 (2011).

46. C. K. Hong, Z. Y. Ou, L. Mandel, *Phys. Rev. Lett.* **59**, 2044 (1987).

47. T. Legero, T. Wilk, M. Hennrich, G. Rempe, A. Kuhn, *Phys. Rev. Lett.* **93**, 070503 (2004).

48. M. B. Plenio, *Phys. Rev. Lett.* **95**, 090503 (2005).

49. We thank Tim Hugo Taminiau, Earl Campbell, David DiVincenzo, Mikhail Lukin, Tracy Northup, Lieven Vandersypen and Stephanie Wehner for fruitful discussions. We acknowledge support from the EPSRC National Quantum Technology Hub in Networked Quantum Information Technology (SCB), the Netherlands Organisation for Scientific Research

(NWO) through a VICI grant (RH), and the European Research Council through a Starting Grant (RH). Data contained in this paper are archived at https://doi.org/10.4121/uuid:9ccff914-1a8c-4d64-9ac3-b06122b86c5e.

List of Supplementary Materials:

Materials and Methods

Table S1 - S4

Fig. S1 - S10

References (45-48)

Fig. 1: Entanglement distillation on a quantum network. (**A**) Working principle: a remote entangled state of higher quality (right) is distilled via local operations and classical communication from several lower-quality states (left) that are shared between remote qubits (depicted as colored spins). (**B**) Protocol overview. Each network node consists of a communication qubit (purple) and a memory qubit (yellow). First, the communication qubits are prepared in a remote entangled state by generating entanglement between a photon (red wave packet) and the spin, interfering the optical modes on a beam splitter (gray cube) and subsequently detecting a single photon ①. Next, the remote entangled state (purple waves represent entanglement) is swapped onto the memory qubits ②, followed by another round of entangled state generation ③. Finally, local operations (black circuit) distill a state of higher fidelity ④. (**C**) Gate circuit implementing steps ①-④. We include the photonic modes of each setup (red wave packets) in which a qubit is encoded such that vacuum and a single photon represent $|0\rangle$ and $|1\rangle$ respectively. Entanglement between the electron spin and photonic mode is experimentally realized by an optical π-pulse (depicted as CNOT symbol). The photonic Bell-state projection $|\Psi^{\pm}\rangle\langle\Psi^{\pm}|$ is probabilistically realized by a beam splitter and subsequent detection of a single photon. Dashed-bordered gates indicate phase-shifts of the memory due to free evolution during entangling attempts. Colored boxes indicate logical blocks of the circuit and are used throughout the manuscript.

Fig. 2: Benchmarking local control. (**A**) Gate circuit for entanglement generation within one node. All local operations of the distillation circuit are used to generate an entangled state between communication and memory qubit. Color coding of local operations corresponds to Fig. 1C. (**B**) Absolute value of the real part of the local density matrix obtained via sequential QST (see Fig. S9 and (*30*)). We find fidelities with the desired entangled state of $0.96(1)$ (node A) and $0.98(1)$ (node B). Transparent bars give the values of the ideal state.

Fig. 3: Quantum state storage during entangling operations. (**A**) Real-time feedback circuit for memory qubits. We initialize memory A/B, which then experiences a phase-shift of $-\varphi_{A/B}$ per executed entangling attempt. After reinitialization of the communication qubit, the distillation step of the protocol is performed (Fig. 1C). Blue-rimmed gate indicates the feedback. (**B**) Memory state as a function of the number of entangling attempts. The oscillation observed without feedback (orange) is successfully compensated (blue) by the feedback. Solid lines are fits to the data. (**C**) Memory lifetime of node A (triangles) and node B (circles). We initialize the memory in one of the six cardinal states of the Bloch sphere (see right panel), sweep the number of entangling attempts, apply feedback, and read-out the expectation value that is relevant for the estimation of the state fidelity with the initial cardinal state. Note that all fidelity-irrelevant expectation values are set to zero, i.e. we depict projections of the state onto the respective axis in the Bloch sphere picture. The average state fidelities are separately plotted for phase-sensitive superposition states (blue) and phase-insensitive eigenstates (green). Blue solid lines depict a generalized exponential fit (*30*). The decay is limited by the stochastic repumping process, microwave pulse errors and/or environmental dephasing. The color gradient of the left and right panel match to facilitate comparisons. Error bars represent one standard deviation.

Fig. 4: Experimental realization of entanglement distillation. (**A**) Two-qubit density matrices for $\theta = \pi/6$ and a maximum of 50 entangling attempts in the second round. Right panel: different detectors clicked. Left panel: the same detector clicked twice. We find a fidelity with the ideal state of $0.65(3)$ for both states. Transparent bars represent the ideal state. (**B**) Fidelity with the ideal state as a function of θ for a maximum of 50 entangling attempts in the second round. Blue data is the two-memory state fidelity. Dashed lines are derived from our

model (*30*). Purple data is the measured raw state fidelity on the communication qubits. Solid orange (purple) line is the modeled fidelity of the raw state on the memories (communication qubits) that would be obtained if the initial internal phase was known. The memory state is calculated for the average number of entangling attempts until success (25). The orange shaded region is the modeled memory fidelity for minimal (0 attempts) and maximal (50 attempts) dephasing. The θ-dependence of the distilled state fidelity is explained by the finite probability of misidentifying a separable state (the presence of which scales with θ) as a successfully distilled entangled state due imperfect quantum control and decoherence of the stored state. Fidelities were obtained by measuring the expectation values $\langle \hat{X}\hat{X} \rangle$, $\langle \hat{Y}\hat{Y} \rangle$ and $\langle \hat{Z}\hat{Z} \rangle$. We denote the Pauli operators as $\hat{X}$, $\hat{Y}$ and $\hat{Z}$. (**C**) State decay for $\theta = \pi/6$. Data are binned according to the number of second entanglement generation attempts until success. Shown are the state fidelity (blue) and the absolute value of the relevant expectation values. The dashed lines are derived from our theoretical model (see Fig. S5). Error bars represent one standard deviation.

Fig 5: Ebit rate comparison. Ebit rate as a function of excitation angle θ. The blue data is derived from the measured success rates and state fidelity over the entire data set (see Fig. S8). The blue dashed line is the estimated ebit rate for distillation including the overhead of local operations. The solid (dashed) orange line gives the estimated ebit rate of a standard two-photon protocol including (excluding) imperfections. All data are averaged over both detection signatures. Error bars represent one standard deviation.

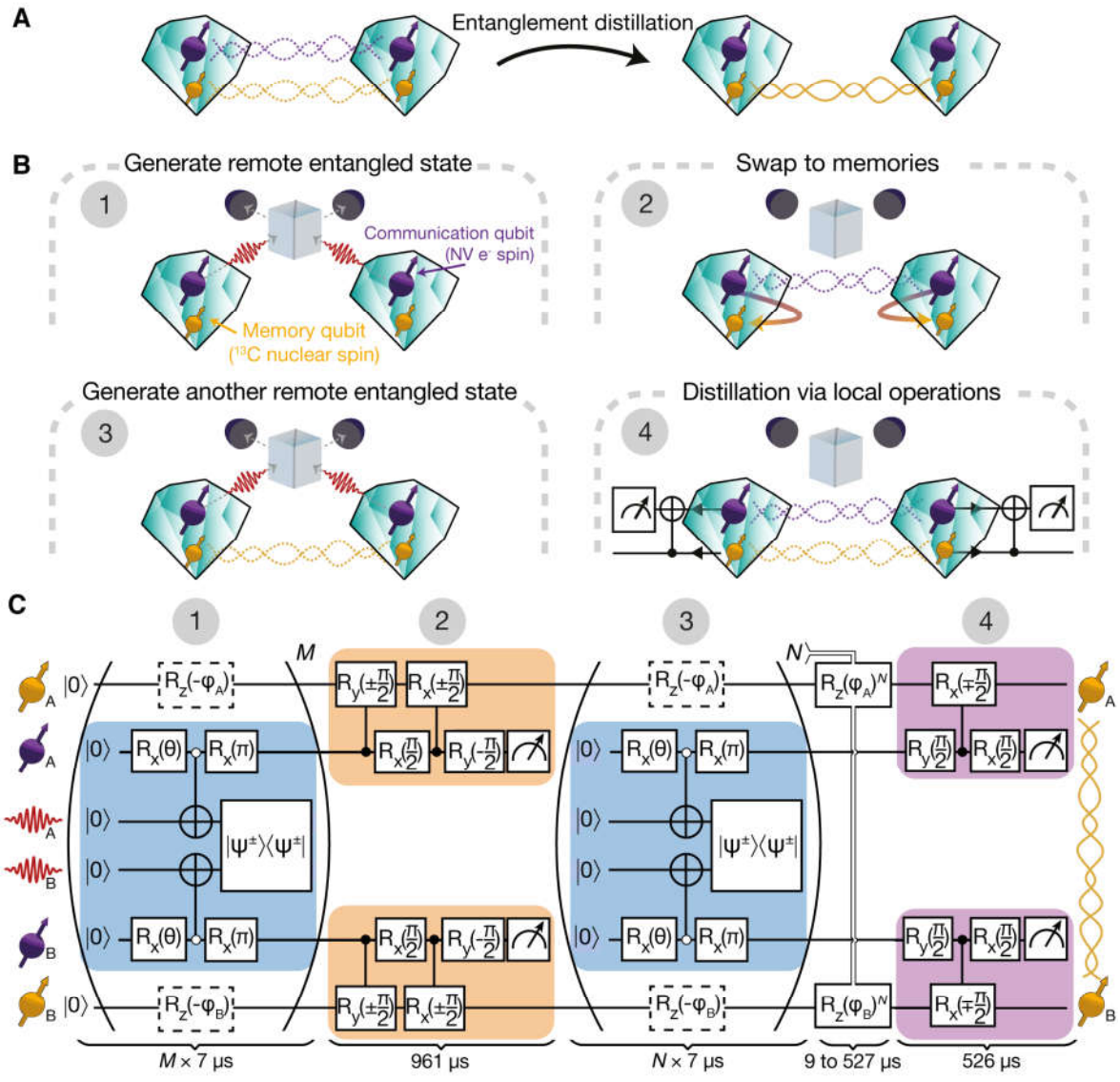

Kalb et al., Fig. 1

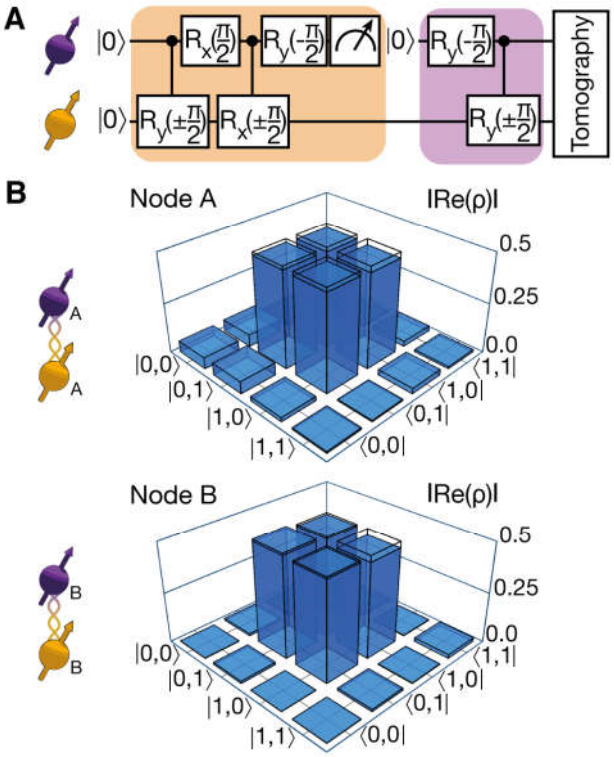

Kalb et al., Fig. 2

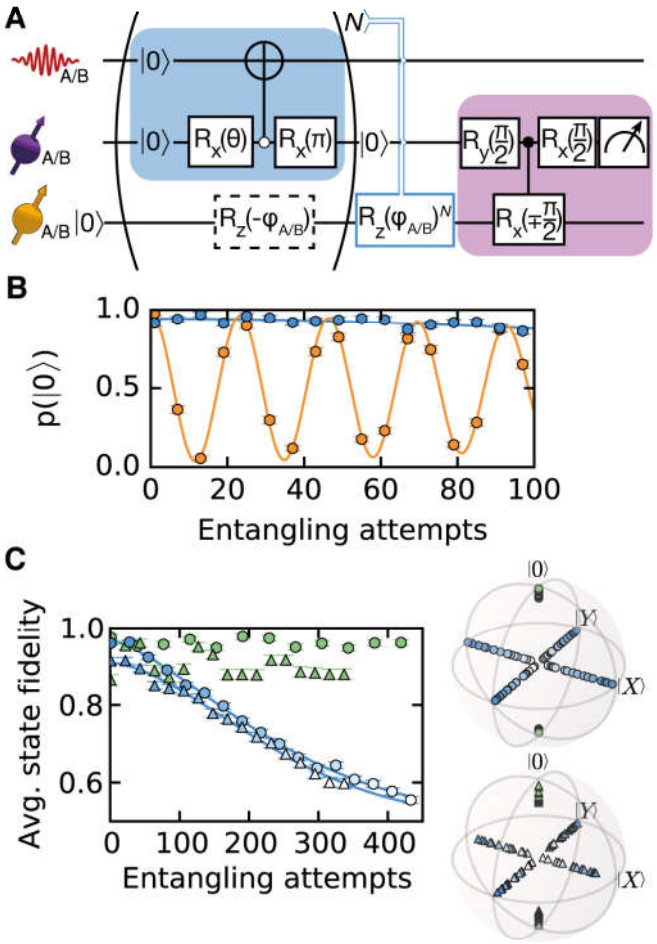

Kalb et al., Fig. 3

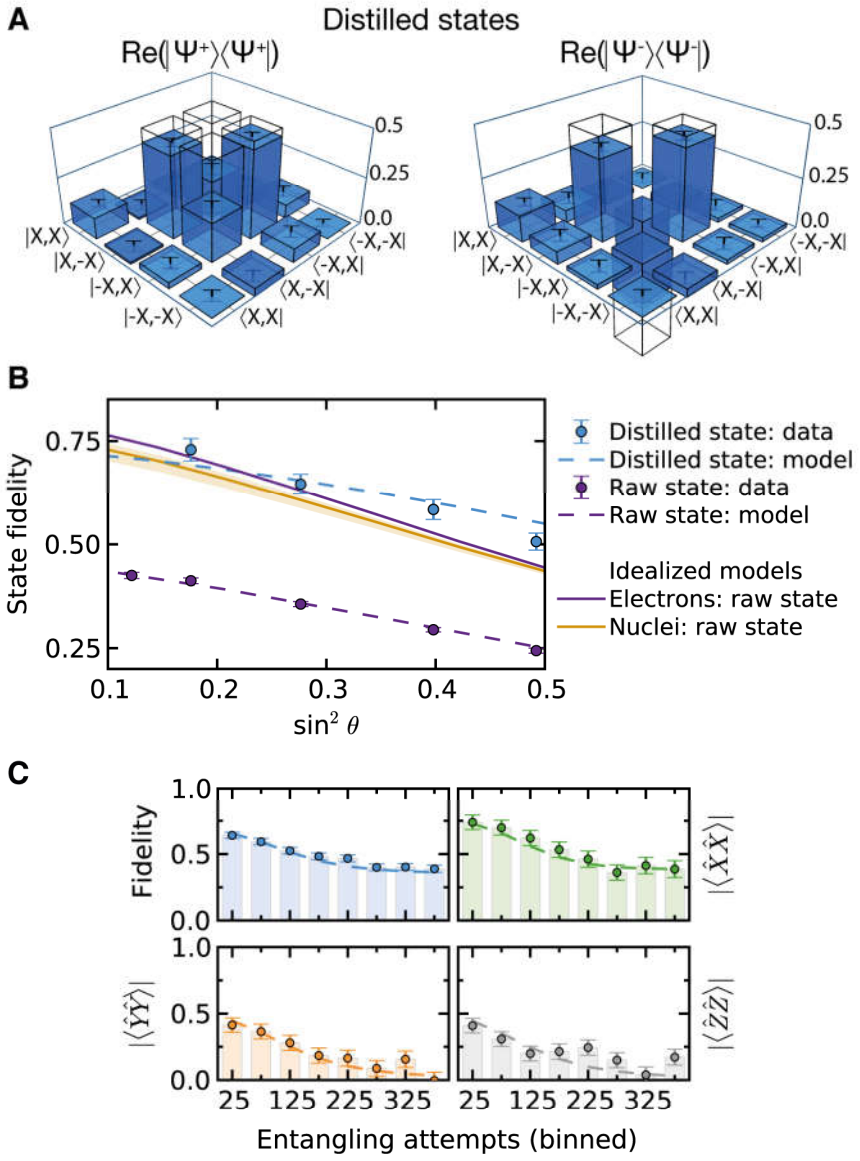

Kalb et al., Fig. 4

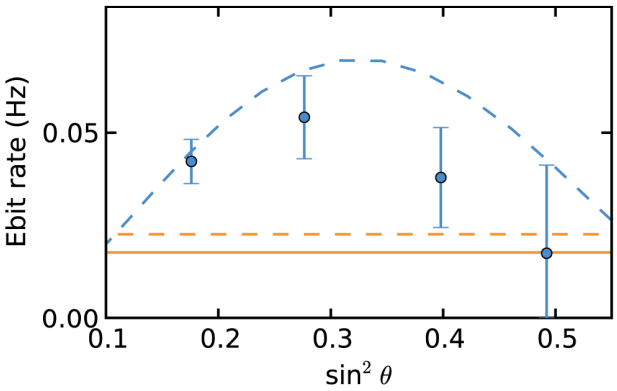

Kalb et al., Fig. 5

Supplementary Materials for

Entanglement Distillation between Solid-State Quantum Network Nodes

N. Kalb,[1,2,*] A. A. Reiserer,[1,2,†] P. C. Humphreys,[1,2,*] J. J. W. Bakermans,[1,2] S. J. Kamerling,[1,2] N. H. Nickerson,[3] S. C. Benjamin,[4] D. J. Twitchen,[5] M. Markham,[5] and R. Hanson[1,2]

[1] *QuTech, Delft University of Technology, P. O. Box 5046, 2600 GA Delft, The Netherlands*
[2] *Kavli Institute of Nanoscience, Delft University of Technology, P. O. Box 5046, 2600 GA Delft, The Netherlands*
[3] *Department of Physics, Imperial College London, Prince Consort Road, London SW7 2AZ, U.K.*
[4] *Department of Materials, University of Oxford, Parks Road, Oxford OX1 3PH, U.K.*
[5] *Element Six Innovation, Fermi Avenue, Harwell Oxford, Didcot, Oxfordshire OX11 0QE, U.K.*

This PDF file includes

- Materials and Methods
- Figs. S1 to S10
- Tables S1 to S4

* These authors contributed equally
† These authors contributed equally; Present address: Max-Planck-Institute for Quantum Optics, Hans-Kopfermann-Str. 1, 85748 Garching, Germany

MATERIALS AND METHODS

A. Experimental design

We use chemical-vapour-deposition homoepitaxially grown diamonds of type IIa with a natural abundance of carbon isotopes. Both diamonds have been cut along the $\langle 111 \rangle$ crystal axis and were grown by Element Six. They are situated in home-built confocal microscope setups within closed-cycle cryostats (4 K, Montana Instruments) separated by two meters. We additionally employ a magnetic field (Node A: 418.248(5) G; node B: 413.980(5) G) approximately aligned with the NV symmetry axis in both setups by placing a permanent magnet within the respective sample chamber and compensating slight alignment-deviations with additional permanent magnets from the outside (few cm distance). Microwave pulses are applied via a gold stripline (thickness of 200 nm) that has been deposited onto the surface of the sample. We shape these pulses to a Hermite amplitude envelope for robustness against qubit frequency detunings ($\approx$ MHz) such as arising from the hyperfine interaction with the host nitrogen nuclear spin *(28)*. To generate short optical excitation pulses, we use an electro-optic modulator (Jenoptik) in a homebuilt, temperature stabilized, enclosure which, in conjunction with an upstream acousto-optic modulator (Gooche & Housego), creates a laser pulse with high on/off ratio and Gaussian temporal envelope. This pulse is split into two using a polarization maintaining fiber beam splitter (Evanescent Optics) for excitation of both NV centers (see also Section E). Optical transition frequencies of each NV center are tuned by applying voltages to gold electrodes on the diamond surface.

We employ a single-layer anti-reflection coating for 637 nm light (Al_2O_3) and solid immersion lenses around the position of the NVs to increase optical collection efficiencies. This in conjunction with the cryogenic environment allows for spin-selective optical read-out of the NV electron spin in a single-shot via the optical E_x (E_y) transition on node A (node B). We measure read-out fidelities of 0.9379(6) (0.8985(7)) for the bright $|m_s = 0\rangle \equiv |0\rangle$ ground-state and 0.9932(2) (0.9962(1)) for the dark $|m_s = +1\rangle \equiv |1\rangle_{\mathrm{A}}$ ($|m_s = -1\rangle \equiv |1\rangle_{\mathrm{B}}$) state on node A (node B). These values are subsequently used to correct for read-out errors of the electron spins in state tomography measurements. Node A additionally uses adaptive optics to compensate for imperfections in the solid immersion lens, which leads to an improved collection efficiency of zero-phonon-line (ZPL) photons *(28)*.

We utilize each electron spin to control an adjacent nuclear spin ($I = \frac{1}{2}$) associated with a ^{13}C atom in the diamond lattice via dynamical decoupling sequences that are resonant with the electron-nuclear dynamics, optimizing the gate parameters to maximize the fidelity of our operations. The parameters for a full entangling operation between nuclear and electron spin are given in Table S1. Furthermore we characterize the strength of the magnetic hyperfine interaction between nuclear spin and electron as well as nuclear dephasing times with the electron spin idling in one of the two relevant states ($|0\rangle$ or $|1\rangle$). The decay of the memories when performing entangling attempts are best fit with exponential functions of the form $e^{-(t/T)^n}$ with T the $1/e$ decay constant and with exponents $n = 1.7(1), 1.48(5)$ for nodes A and B respectively. We correct for tomography errors on the nuclear spin state by employing previously developed methods that rely on a symmetric initialization and read-out of the respective nuclear spin *(26, 44)*. The measured quantities are given in Table S1.

B. Experimental sequence

Remote entangled electron spin states are generated by initializing the superposition state $|\theta\rangle$ on both sides (we use a 2 μs long repumping laser pulse followed by a microwave pulse) and subsequent

optical excitation from a common laser source which guarantees relative frequency-stability. The sequence duration is $7\,\mu$s. A photo-detection event heralds the desired raw state of Eq. (2). We obtain single-photon detection probabilities of $p_{\mathrm{a}} = 8 \cdot 10^{-4}$ ($p_{\mathrm{b}} = 4 \cdot 10^{-4}$) for node A (node B). A final microwave π-pulse preserves electron coherence and decouples the magnetic hyperfine interaction with the memory *(27)*.

Generating remote entangled states with low detection efficiencies requires complex logic operations to limit overhead and guarantee a time-efficient execution of the sequence. We implement charge resonance checks for pre-selection of and feedback on the current NV emission frequencies as well as multiple logical stages in the sequence at which both nodes communicate local success or failure. Combined success events advance the sequence one step further whereas failure causes a restart. A schematic of the electrical wiring is depicted in Fig. S1. Figure S2 gives an overview of all communication steps between the involved instruments.

C. Confirmation herald for a high fidelity swap

The fidelity of the local swap operation is improved by constructing a confirmation herald. Prior to the swap the memory is initialized in the phase-insensitive eigenstate $|0\rangle$ which gets mapped onto the fluorescing electron state $|0\rangle$ by the applied gate sequence. Measuring the electron in the state $|0\rangle$ by detection of a photon after the swap sequence therefore suppresses infidelities at negligible cost in efficiency (measured success probability of 0.89(1)).

D. Temporal filtering & CPLD timing

We determine the relative timing of clicks originating from avalanche photodiodes (APDs) 1 and 2 by creating histograms of all detection events registered from each APD by the TDC. The maximum of the auto-correlation between these histograms indicates the timing delay at which the two temporal distributions are best overlapped.

Once this timing is determined, we fit a Gaussian profile to the beginning of the histogram of all overlapped data (Fig. S3). This Gaussian profile is known to closely correspond to our excitation pulse profile. We use this fit to estimate the point in time beyond which the ratio between photons from the excitation laser and the integrated residual NV emission is less than 0.001. This independently determined time set the beginning of the temporal filter in our analysis of the distillation results. We choose this conservative criterion in order to mitigate any potential impact of non-Gaussian tails in the laser profile.

In order to minimize the impact of dark counts, we set the end of the temporal filter to be 40 ns after the start of the window. This filtering is chosen because, for times longer than 40 ns after the excitation pulse, the ratio between dark counts and NV photon detections is estimated to increase above 0.1 for the most sensitive case ($\theta = \pi/8$). A live temporal filter through the CPLD (see Figs. S1 and S2) allows us to exclude 36.6 % of all events on-the-fly.

E. Optical transition frequencies of the NV in a magnetic field

Lateral crystal strain modifies the eigenstates and respective eigenenergies of the NV excited electronic states. Fig. S4 shows the optical transition frequencies ω_{Ex} for $|m_s = 0\rangle \rightarrow |E_x\rangle$ and $\omega_{\pm 1}$ for the transitions $|m_s = \pm 1\rangle \rightarrow |A_1\rangle$, as a function of lateral strain. The transition $|m_s = 0\rangle \rightarrow |E_x\rangle$ is of particular interest as it remains spin conserving even under large lateral strain fields (no deterioration was found for strain induced frequency shifts up to 5 GHz). Without magnetic field

the ground states $|m_s \pm 1\rangle$ are degenerate and $\omega_{+1} = \omega_{-1}$. In this case, at a lateral strain-induced frequency shift around 3.5 GHz ω_{Ex} and $\omega_{\pm 1}$ are nearly degenerate which hampers the quality of spin-photon entanglement. Applying a sufficiently large magnetic field along the NV axis splits the ground states due to the Zeeman effect; therefore ω_{Ex} is degenerate with ω_{+1} and ω_{-1} in distinct strain regimes and there is always a choice of qubit states in the ground state triplet of the NV center that allows for high-quality spin-photon entanglement. In our experiment node A operates at a lateral strain-induced frequency shift of $\sim 4\,\mathrm{GHz}$ such that we choose $|1\rangle \equiv |m_s = +1\rangle$. These considerations are not a factor for node B, as in this case we are using the transition $|m_s = 0\rangle \rightarrow |E_y\rangle$.

F. Distillation protocol

We entangle distant NV spins by employing single photons as flying qubits in a probabilistic measurement-based entanglement (MBE) protocol. After initializing each NV in the $|m_s = 0\rangle$ ground state, which we will label $|0\rangle$, a microwave pulse is used to rotate the spin into a superposition of this state and one of the $|m_s = \pm 1\rangle$ states, here labeled $|1\rangle$. This prepares each NV in the state

$$|\theta\rangle = \sin\theta\,|0\rangle - i\cos\theta\,|1\rangle\,. \tag{1}$$

Subsequent spin-selective resonant excitation of the NVs leads to the emission of a single photon if the NV is in the $|0\rangle$ state, creating spin-photon entangled states at each node. These single photons are transmitted to a central node and subsequently interfered on a beam splitter. In the ideal case, detection of a single photon after this beam splitter projects the NVs onto the entangled state $|\Psi^{\pm}\rangle = -i(|01\rangle \pm |10\rangle)/\sqrt{2}$ (where the sign depends on which detector clicked).

We do not stabilize the phase of the excitation laser at the position of the NVs, nor the optical path length traversed by the emitted photons from the NVs to the central node. These differences between the two optical paths apply an unknown phase ϕ to the entangled state. In addition, the NVs only emit photons 3% of the time in the usable zero-phonon line (ZPL), and the optical channels have finite transmissivities. This leads to a reduced probability p_{d} of successfully detecting a single photon given that one of the NVs was in the $|0\rangle$ state. These dominant imperfections mean that we actually produce the state

$$\rho_{\mathrm{raw}}(\phi) = \eta\left|\Psi^{\phi}\right\rangle\left\langle\Psi^{\phi}\right| + (1-\eta)\,|00\rangle\langle 00|\,, \tag{2}$$

where $\left|\Psi^{\phi}\right\rangle = (|01\rangle + e^{\mathrm{i}\phi}\,|10\rangle)/\sqrt{2}$ and η depends on both θ and p_{d}.

Each communication qubit is flipped by applying $R_{\mathrm{x}}(\pi)$ as part of our dynamical decoupling sequence and then (following *(8, 34)*) swapped onto local memories at each node. This allows us to reuse the NVs to produce a second entangled state between the nodes. Upon success, our overall state is then given by $\rho_{\mathrm{raw}}(\phi_2) \otimes \rho'_{\mathrm{raw}}(\phi_1)$, where ϕ_2 and ϕ_1 depend on the phase differences at the two different times that the states were created (for pedagogical clarity, here we assume that the same detector clicked). Due to the particular swapping operation we employ, the memory state $\rho'_{\mathrm{raw}}(\phi_1)$ is a rotated version of the initial state $\rho_{\mathrm{raw}}(\phi_1)$, such that $\rho'_{\mathrm{raw}}(\phi_1) = U\rho_{\mathrm{raw}}(\phi_1)U^{\dagger}$. Therefore, for readability, in the following text we redefine the memory qubit states in a rotated basis such that the states $|0\rangle_m$ and $|1\rangle_m$ are superpositions of the energy eigenstates $|0\rangle$ and $|1\rangle$ that are employed in the main text.

$$
\begin{aligned}
(|10\rangle_c + e^{i\phi_2}|01\rangle_c) \otimes (|10\rangle_m + e^{i\phi_1}|01\rangle_m) &\rightarrow (|11\rangle_c + e^{i\phi_2}|00\rangle_c) \otimes |10\rangle_m + e^{i\phi_1}(|00\rangle_c + e^{i\phi_2}|11\rangle_c) \otimes |01\rangle_m\,, \\
(|10\rangle_c + e^{i\phi_2}|01\rangle_c) \otimes |11\rangle_m &\rightarrow (|10\rangle_c + e^{i\phi_2}|01\rangle_c) \otimes |11\rangle_m\,, \\
|11\rangle_c \otimes (|10\rangle_m + e^{i\phi_1}|01\rangle_m) &\rightarrow |10\rangle_c \otimes |10\rangle_m + e^{i\phi_1}|01\rangle_c \otimes |01\rangle_m\,, \\
|11\rangle_c \otimes |11\rangle_m &\rightarrow |11\rangle_c \otimes |11\rangle_m
\end{aligned} \tag{3}
$$

Measurement of both communication qubits in the $|00\rangle_c$ state heralds successful distillation. For a balanced superposition state ($\theta = \pi/4$) and high photon loss ($p_\mathrm{d} \ll 1$), in which case $\eta = 1/2$, the distillation succeeds with probability $\frac{1}{8}$. It can be seen that this projects the memories into the pure state $\frac{1}{\sqrt{2}}(e^{i\phi_1}|01\rangle_m \otimes + e^{i\phi_2}|10\rangle_m)$, and so the $|11\rangle\langle 11|$ contamination has been removed.

In addition, if the phase drift over the duration of the experiment is sufficiently small, such that $\phi_1 \approx \phi_2$, one obtains the desired entangled state $|\Psi^+\rangle = \frac{1}{\sqrt{2}}(|01\rangle_m + |10\rangle_m)$. If different detectors clicked in the first and second rounds of entanglement generation, it can be easily shown that the resulting state is instead $|\Psi^-\rangle = \frac{1}{\sqrt{2}}(|01\rangle_m - |10\rangle_m)$.

In reality, our experiment has further experimental imperfections beyond optical phase drifts, and so the state that is actually produced by the distillation protocol deviates from this ideal entangled state. In our experiment, the primary imperfections are given in Table S3, along with independent estimates of their magnitudes. We incorporate these parameters into an analytical model of the experiment, as is outlined in the following section.

The independently estimated parameters are not sufficient to completely explain the obtained state fidelities. We therefore introduce two phenomenological parameters: an initial amplitude damping implemented via a dephasing operation ($p = 0.08$) on the memory qubits and additional interferometric drift of the setup per entangling attempt. We fit our model to the combined dataset for all excitation angles. The resulting fit (3.4 mrad per entangling attempt) suggests an increased drift of the relative phase between both raw states which could be caused by a deviating interferometric stability at the time of data acquisition. In order to make a conservative comparison, these additional experimental infidelities are excluded for the modeled stored raw state that we compare with the distilled state in Fig. 4B of the main text. Fig. S5 shows the state decay for all measured superposition angles and the result from fitting the model to the combined data set.

G. Experimental model

1. *Raw state*

The raw entangled state in our model is given by

$$
\rho_\mathrm{raw} = p_{00}\,|00\rangle\langle 00| + p_{11}\,|11\rangle\langle 11| + \left|\Psi^\pm\right\rangle\left\langle\Psi^\pm\right| \tag{4}
$$

where

$$
\left|\Psi^\pm\right\rangle\left\langle\Psi^\pm\right| = \begin{pmatrix}
\frac{1}{2}p_\mathrm{s}(p_{01}+p_{10}) & 0 & 0 & 0 \\
0 & p_{01}(1-p_\mathrm{s}) & \pm\sqrt{V\,p_{01}\,p_{10}}\,(1-p_\mathrm{s})e^{i\phi} & 0 \\
0 & \pm\sqrt{V\,p_{01}\,p_{10}}\,(1-p_\mathrm{s})e^{-i\phi} & p_{10}(1-p_\mathrm{s}) & 0 \\
0 & 0 & 0 & \frac{1}{2}p_\mathrm{s}(p_{01}+p_{10})
\end{pmatrix}. \tag{5}
$$

This state is parametrized by

$$
\begin{aligned}
p_{11} &= 2\cos^4\theta\, p_{\rm dc}\,(1-p_{\rm dc}) \\
p_{10} &= \sin^2\theta\,\cos^2\theta\,((1-p_{\rm dc})^2\,p_{\rm d2} + 2\,p_{\rm dc}(1-p_{\rm dc})(1-p_{\rm d2})) \\
p_{01} &= \sin^2\theta\,\cos^2\theta\,((1-p_{\rm dc})^2\,p_{\rm d1} + 2\,p_{\rm dc}(1-p_{\rm dc})(1-p_{\rm d1})) \\
p_{00} &= \sin^4\theta\,((1-p_{\rm dc})^2(p_{\rm d1}(1-p_{\rm d2}) + p_{\rm d2}(1-p_{\rm d1})) + 2(1-p_{\rm dc})\,p_{\rm dc}(1-p_{\rm d1})(1-p_{\rm d2})).
\end{aligned} \tag{6}
$$

2. Protocol

We model the swap gate that transfers the entangled state to the nuclear spins at each node by assuming that this gate causes random two-qubit Pauli noise with a probability $2 \times p_{\rm gate}$. As in the experiment, this swap gate stores the entangled state in a rotated basis, such that the initial electronic state is transformed by a Hadamard gate as it is stored.

After this swap, the stored state experiences dephasing noise due to the second round of entanglement attempts. This is modeled by applying a $R_{\rm z}(\pi)$ rotation independently to each of the stored states with a probability $p_{\rm m}$. For Gaussian dephasing noise (such as decoherence), in which the fidelity of a stored state degrades as $F = \frac{1}{2}(1 + e^{-\frac{n^2}{2\tau^2}})$, $p_{\rm m} = 1 - F \equiv \frac{1}{2}(1 - e^{-\frac{n^2}{2\tau^2}})$. For exponential damping noise (such as the stochastic repumping process used to reset our NV spins *(27)* , $p_{\rm m}$ is given by $\frac{1}{2}(1 - e^{-\frac{n}{\tau}})$. Besides the induced dephasing due to the electron spin reset, we find that our feedback resolution is limited by systematic drifts of the required feedback phase per entangling attempt. Analyzing all calibration data results in an additional phase uncertainty of $0.87(3)\,$mrad per entangling trial per node which is taken into account via a Gaussian decay channel.

We introduce a second raw entangled state, modeling the optical phase drift since the first state was generated by applying a $R_{\rm z}(\pi)$ rotation to one of the qubits with a probability determined by the expected phase drift $\Delta\phi$ per attempt (Section I).

The distillation operation consists of another two-qubit gate between the electron and the nuclear spin at each node, and again is modeled by assuming random two-qubit Pauli noise, this time with a probability $p_{\rm gate}$. Finally, we calculate the state of the nuclear spins after a noisy measurement of the electron spin, with a failure probability given by $p_{\rm proj}$.

H. Two-photon quantum interference

We are able to estimate the degree of indistinguishability between the single photons emitted by each NV by aggregating the full set of detection events from the distillation data set. Using the same temporal filtering as for the distillation analysis, we calculate the number of events within this data set in which both APDs detect a photon within the same entanglement generation element. This is normalized by calculating the number of events in which one APD clicked in a given entanglement generation element, while the other APD clicked in the next entanglement generation element.

For fully distinguishable single-photon emission and balanced emission probabilities, the ratio r between coincident clicks to clicks in successive elements should be 0.5, while for fully indistinguishable photons no coincident clicks will be detected due to two-photon Hong-Ou-Mandel quantum interference *(46)*. This is because this quantum interference effect ensures that the two photons will always emerge from the same port of the beam splitter, and so both APDs will never click during the same round. For partially indistinguishable photons and again assuming balanced emission probabilities, r is related to the wave function overlap $V = |\langle\psi_a|\,\psi_b\rangle|^2$ by $V = (1 - 2\,r)$.

Incorporating the effect of the known imbalance in emission probabilities in our experiment, we find $V = 0.72(3)$. This is substantially lower than measured in Refs. *(24, 28)* . We hypothesize that this is due to fast spectral diffusion of one of our NVs, which is not picked up by our charge resonance checks as they confirm resonant conditions on a time scale of 100μs. In the future further insight into the emission properties of single NVs could be obtained by interfering photons from a single emitter in an unbalanced interferometer *(47)*.

I. Phase stability

As mentioned in Section G 2, in order to create the initial spin-photon entanglement, resonant laser pulses are used to selectively excite the $|m_s = 0\rangle$ state to a higher level; this excited state then spontaneously decays, emitting a single photon. In this way, the photon-number occupation of the emission optical mode becomes entangled with the state of the NV. This resonant excitation process imprints the phase of the excitation laser onto the resulting spin-photon state. As the optical mode propagates towards the beam splitter, it also picks up an additional phase that depends on the optical path length that it traverses. After the optical modes from each NV interfere on the beam splitter and a photon is detected, the resulting spin-spin entangled state has a phase ϕ that depends on the total phase difference between the two spin-photon states.

Since we derive the resonant excitation pulses from the same laser, the full setup effectively acts as an optical interferometer (Fig S7A), starting from where the excitation pulses are split, and ending at the beam splitter at which the photons are interfered. The phase sensitivity of the resulting spin-spin entangled state is the same as for classical light traversing the same paths, but reflecting off of the NV sample instead of exciting the NV. By probing the stability of the interferometer using classical light, we can therefore determine the expected difference between ϕ_1 and ϕ_2 for subsequent entangled states. This allows us to determine how much the interferometer phase stability will impact the fidelity of the resulting distilled state.

Fig. S7B shows measurements of the output intensity of one port of the beam splitter, measured using a photodiode. As the interferometer is not phase stabilized, the output fluctuates over time. The noise spectral density for this signal is shown in Fig. S7C. Several clear resonances can be seen below 1 kHz; these dominate the dynamics of the interferometer.

A useful measure for quantifying the phase stability of the interferometer is the standard deviation $\Delta\phi$ of the phase difference $\delta\phi(\tau) = \phi(t + \tau) - \phi(t)$ between two sample points separated by a fixed time difference τ, measured for all t in the sample. This is plotted in Fig. S7D. As can be seen, the standard deviation $\Delta\phi$ grows rapidly for the first millisecond, and then oscillates more slowly. These oscillations are caused by several resonant frequencies that dominate the noise spectrum of the interferometer, as is shown in Fig. S7C.

Once the first entangled state is created, the swap operations take 0.961 ms. For the data of Fig. S7, this would lead to an initial phase deviation of $\Delta\phi \approx 0.18$ rad. Each entanglement generation attempt during the second stage takes 7μs. We do not try more than 500 times to generate an entangled state the second time, and so the phase deviation would not increase beyond $\Delta\phi \approx 0.24$ rad. Therefore, for the data in Fig. S7, we find an estimated dephasing probability of 0.018. Since the interferometer is not monitored during the experiment, these estimates can only serve as a guide. In our modeling we use the phase stability as a free parameter, fitting a linearly increasing phase deviation with $\Delta\phi = 0.49$ rad after 1 ms, which is larger but of the same order as that measured in Fig. S7.

J. Ebit rate estimates

1. Distillation

From our experimental data, we can determine the total number of successful events n_s, as well as the total number of entangling attempts made n_a. From these numbers and the duration of an entanglement attempt $t_e = 7\,\mu$s, we can estimate the instantaneous rate $r = n_s/(n_a t_e)$ at which the protocol succeeds (i.e. the rate assuming that both NVs are on resonance, a condition which is necessary for any network protocol). As shown in Fig. S8A, this rate is a function of the superposition angle θ.

The distillable entanglement of a state ρ is upper bounded by its logarithmic negativity $E_N(\rho)$, an easily computable entanglement measure *(48)*. $E_N(\rho)$ is determined by the sum of the singular values of the partial transpose of ρ. We do not have access to the full density matrix ρ for all of the θ values that we measure. However, we can make an estimate of $E_N(\rho)$ by assuming that all off-diagonal elements of the density matrix are zero, apart from the coherence c between $|01\rangle$ and $|10\rangle$. This assumption is supported by our measurements of the density matrix for $\theta = \pi/6$ (shown in Fig. 4A of the main text), in which other off-diagonal terms were indeed negligible. Under this assumption, it is possible to calculate $E_N(\rho)$ using only our measurements of the correlations $\langle \hat{X}\hat{X}\rangle$, $\langle \hat{Y}\hat{Y}\rangle$ and $\langle \hat{Z}\hat{Z}\rangle$. Parameterizing ρ as

$$\rho = \begin{pmatrix} 1-r-p_{11} & 0 & 0 & 0 \\ 0 & r-p_{10} & c & 0 \\ 0 & c^* & p_{10} & 0 \\ 0 & 0 & 0 & p_{11} \end{pmatrix}, \tag{7}$$

$$E_N(\rho) = \log_2\left(r + \frac{1}{\sqrt{2}}\left(\sqrt{\alpha + (1-r)(1-r+\beta)} + \sqrt{\alpha + (1-r)(1-r-\beta)}\right)\right) \tag{8}$$

$$\text{where } \alpha = 2\,|c|^2 + 2p_{11}^2 - 2p_{11}(1-r),$$
$$\beta = \sqrt{4\,|c|^2 + (1-r-2p_{11})^2}.$$

The logarithmic negativity is plotted in Fig. S8B for different values of θ.

Multiplying the success rate by the distillable entanglement gives us the ebit rate. Since the number of ebits available depends on the number of second round entanglement attempts needed to succeed, we carry out this calculation for different sets of our experimental results, binned by the number of second round attempts. We choose bins separated by fifty entangling attempts. This represents a compromise between having enough experimental results in each bin to calculate the correlations with reasonable accuracy, while not averaging too broadly over the different outcomes.

2. Experimental model

Independent measurements allow us to estimate the probabilities of detecting a single photon given that one or other of the NVs was in the $|0\rangle$ state (Table S3). From these probabilities, we can estimate the probability p_1 of an entanglement generation attempt succeeding in the first round of the protocol. This in turn allows us to estimate $p_2 = p_1(1-p_1)^{n-1}$, the probability of a second entanglement event occurring after a specified number of attempts n, given that the first round succeeded. In addition to these parameters, our model (Section G) allows us to predict the

probability of the local distillation gate succeeding, given the overall electron nuclear-spin state resulting from a specified number of second round entanglement generation attempts. Combining these numbers with the probability of a successful read-out after the distillation gate (0.9 on each side) gives us the average number of attempts (and therefore the time) necessary to produce a successful entanglement event. Our model also allows us to directly calculate $E_N(\rho)$ from the simulated density matrix ρ. The rate and E_N predictions of our model are plotted alongside the experimental data in Fig. S8. This information is used to provide the theoretical lines in Fig. 5 of the main text.

3. Comparison to Barrett and Kok protocol

The single-photon detection probabilities can also be used to estimate the rate that would be achieved for a conventional Barrett-Kok (BK) protocol *(36)* running on our experimental apparatus. Given these probabilities (Table S3), the BK success probability is given by $\frac{1}{2}p_{\mathrm{d}1}p_{\mathrm{d}2}$. As each entanglement attempts takes $7\,\mu s$, this gives a rate of 16 mHz.

In order to calculate the number of ebits available for the BK protocol, we assume that the generated state is perfect, apart from a reduced coherence $c = V/2$ resulting from the imperfect indistinguishability V of our photons. In this case

$$\begin{aligned} E_N(\rho) &= \log_2(1 + 2\,|c|) \\ &= \log_2(1 + V). \end{aligned} \tag{9}$$

The estimated rate and number of ebits are combined to give the BK ebit rates shown in Fig. 5 of the main text.

K. Nuclear initialization and read-out sequences

Nuclear spins in each setup are initialized and read-out by employing conditional electron-nuclear gates and single-shot quantum measurements of the electron. Fig. S9 shows all relevant circuit diagrams for initialization and read-out of the nuclei. The directions of the rotations induced on the memory qubits by the controlled $\pm\pi/2$ gates are determined by the communication qubit states.

Besides using established gate circuits for the tomography of single nuclear spins, we employ a sequential tomography for the combined electron-nuclear Bell states of Fig. 2 of the main text. Here, we first rotate the electron spin by applying one of six suitable microwave pulses followed by a single-shot read-out measurement. We continue with the tomography sequence of the nuclear spin if the electron was successfully measured to be in $|m_s = 0\rangle$. This guarantees a high projectivity of the NV spin and allows for the implementation of the nuclear-spin read-out sequence with high fidelity.

L. P-values for distillation

As noted in the main text, successful distillation requires that the distilled state is increased in fidelity as compared to the raw states. In order to provide evidence that this is the case, we calculate P-values for the measured state fidelities shown in Fig. 4B of the main text (replotted in Fig. S10), taking as a null hypothesis that the states do not show an increase in fidelity from the highest fidelity raw state. These P-values are given in Table S4.

Also calculated are the P-values showing evidence for distillation in the most stringent possible case, in which the raw states were generated in a completely stable interferometer with no phase drifts whatsoever (dashed orange line in Fig. S10). In this case the only imperfections on the raw states result from imperfect two-photon quantum interference, imbalanced optical losses, and dark counts. All of these quantities are independently characterized for our experiment.

M. Measured density matrices

For completeness we present all numerical entries of all measured density matrices in this section. The matrices were directly reconstructed from the measurement outcomes via linear inversion. From Fig. 2B of the main text for node A:

$$\begin{pmatrix} 0.06(1) & 0.06(1)+i0.00(1) & 0.02(1)-i0.02(1) & 0.01(1)+i0.00(1) \\ 0.06(1)+i0.00(1) & 0.48(1) & -0.48(1)+i0.00(1) & -0.01(1)+i0.01(1) \\ 0.02(1)+i0.02(1) & -0.48(1)+i0.00(1) & 0.47(1) & -0.03(1)+i0.00(1) \\ 0.01(1)+i0.00(0) & -0.01(1)-i0.01(1) & -0.03(0)+i0.00(1) & -0.01(1) \end{pmatrix}. \tag{10}$$

and node B:

$$\begin{pmatrix} 0.00(1) & 0.01(1)+i0.02(1) & 0.00(1)-i0.02(1) & 0.00(1)+i0.01(1) \\ 0.01(1)-i0.02(1) & 0.51(1) & -0.49(1)-i0.02(1) & -0.01(1)+i0.03(1) \\ 0.00(1)+i0.02(1) & -0.49(1)+i0.02(1) & 0.47(1) & 0.00(1)-i0.02(1) \\ 0.00(1)-i0.01(1) & -0.01(1)-i0.03(1) & 0.00(1)+i0.02(1) & 0.02(1) \end{pmatrix}. \tag{11}$$

The density matrices of Fig. 4A of the main text are given in the following:

$$\begin{pmatrix} 0.11(2) & -0.01(3)+i0.02(3) & 0.03(3)+i0.01(3) & 0.00(3)-i0.02(4) \\ -0.01(3)-i0.02(3) & 0.43(2) & 0.20(3)+i0.03(4) & -0.04(3)-i0.03(3) \\ 0.03(3)-i0.01(3) & 0.20(3)-i0.03(4) & 0.46(2) & 0.07(3)-i0.05(3) \\ 0.00(3)+i0.02(4) & -0.04(3)+i0.03(3) & 0.07(3)+i0.05(3) & 0.00(2) \end{pmatrix} \tag{12}$$

$$\begin{pmatrix} 0.13(2) & 0.06(3)-i0.05(3) & 0.02(3)+i0.05(3) & 0.00(3)+i0.05(3) \\ 0.06(3)+i0.05(3) & 0.40(2) & -0.21(3)+i0.01(3) & -0.04(3)-i0.03(3) \\ 0.02(3)-i0.05(3) & -0.21(3)-i0.01(3) & 0.45(2) & 0.02(3)-i0.01(3) \\ 0.00(3)-i0.05(3) & -0.04(3)+i0.03(3) & 0.02(3)+i0.01(3) & 0.02(2) \end{pmatrix} \tag{13}$$

Numbers in brackets represent one standard deviation.

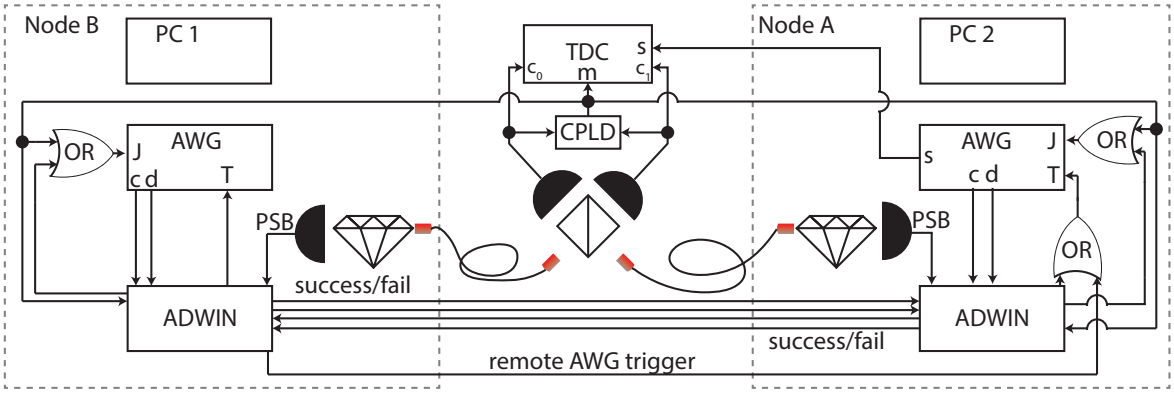

FIG. S1. Control schematic of the experimental setup. Complex programmable logic device (CPLD) outputs a trigger upon detection of a ZPL photon (see Section D for timing). Time-to-digital converter (TDC, PicoQuant HydraHarp 400) with time-tagged channels (c_0 and c_1), a marker for ZPL photon detection events (m), and a sync channel (s). We use microprocessors for decision making (Jäger ADwin Pro II (ADwin)) and arbitrary waveform generators (Tektronix AWG5014c (AWG)) which have input channels for jump (J) and trigger (T) commands. Outputs of the AWGs are used to have the respective local ADwin count the number of entangling events (c) and to determine whether a part of the logical sequence (see Fig. S2) has finished (d). Besides, AWGs and ADwins control all laser and microwave pulses of the respective setup. Personal computers (PCs 1 & 2) are used for sequence programming, hardware control and monitoring during measurements. ADwins record electron-spin readout via luminescence in the phonon sideband (PSB) and communicate success or failure of logical steps within the sequence with a three-way handshake that utilizes two digital input and two digital output channels on each device (success/fail). See Fig. S2 for further details on the sequence. The start of the AWG sequences is triggered via one ADwin to mitigate timing jitter between both AWG outputs.

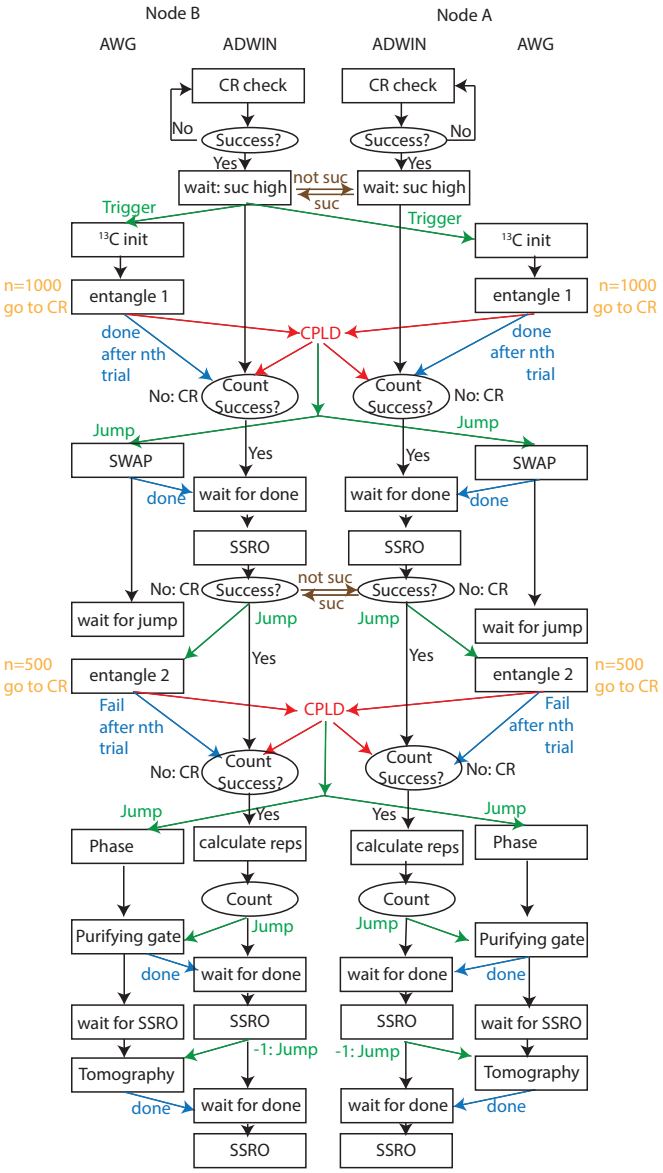

FIG. S2. Logical blocks for the AWG and ADwin of each setup during one round of distillation. For a wire diagram of the experimental logic see Fig. S1. Boxes give logical steps within the sequence (see also Fig. 1C of the main text). Conditional actions and feedback are implied by ellipses. Before each experimental run we verify that both electron spins are on resonance via a charge-resonance (CR) check *(45)*. Unless indicated otherwise, black arrows represent an unconditional advance of the sequence even if no communication signal was received. The absence of a black arrow indicates a restart of the sequence upon failure. We additionally provide a glossary of all used terms in Tab. S2.

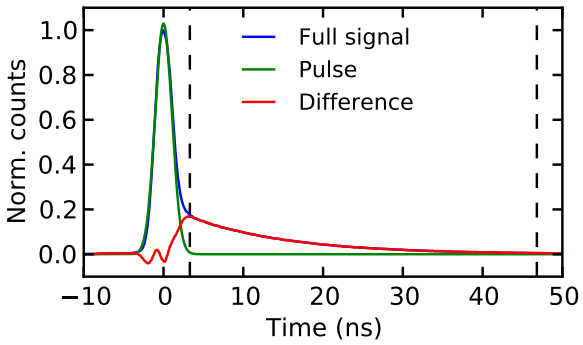

FIG. S3. Plotted in blue is the histogram of the timings of all APD clicks registered by our time-to-digital converter (blue). We fit a Gaussian profile to the beginning of this histogram (green), as this profile is known to closely correspond to the temporal shape of our excitation pulse. The profile of the NV emission (red) is estimated by taking the difference between the full histogram of counts and the photons assumed to originate from the excitation pulse. Dashed lines indicate the beginning and end of the detection window. Time is given with respect to the fitted center of the laser pulse.

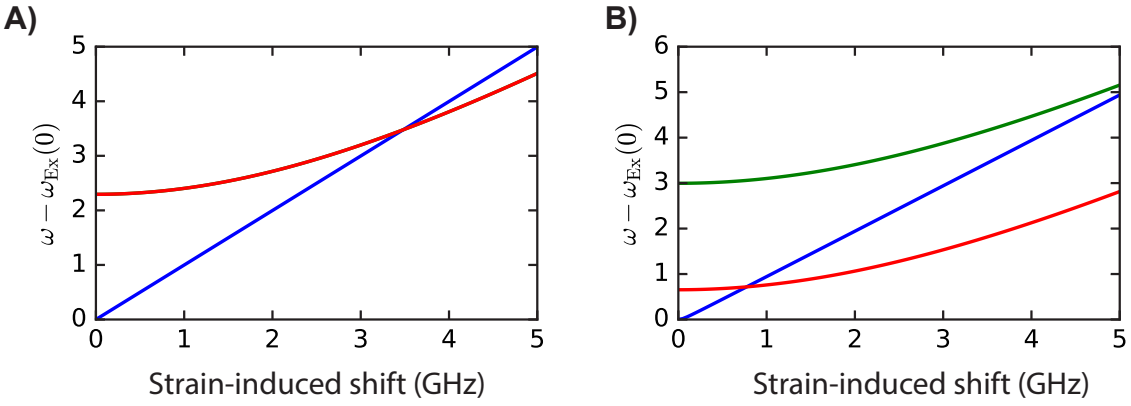

FIG. S4. Optical transition frequencies of the NV electron spin as a function of lateral strain with and without magnetic field. A) without magnetic field and B) with magnetic field along the NV axis ($B = 418.2\,\mathrm{G}$). In the latter case the excitation frequencies $\omega_{\pm 1}$ are no longer degenerate. Blue: transition from $|m_s = 0\rangle$ to $|E_x\rangle$. Red (green): transition from $|m_s = +1\,(-1)\rangle$ to the optically excited state $|A_1\rangle$. Red and green lines overlap in panel A.

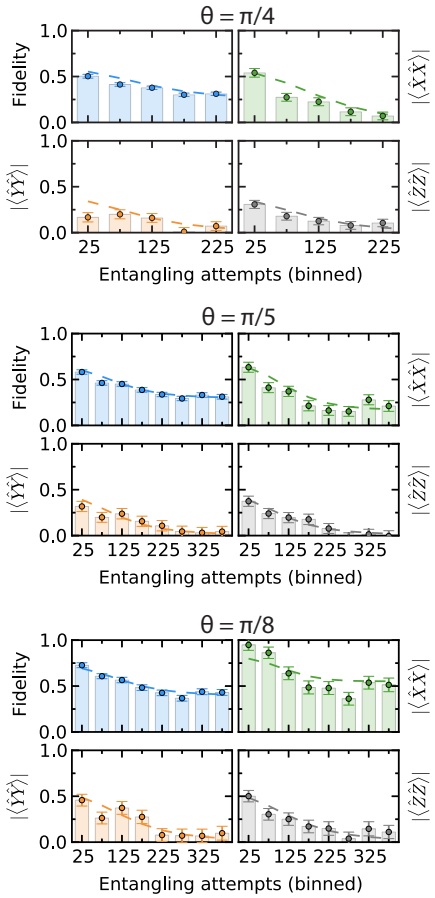

FIG. S5. Modeled (dashed lines) and measured correlations and state fidelities for all remaining excitation angles. See Fig. 4C of the main text for the data of $\theta = \pi/6$.

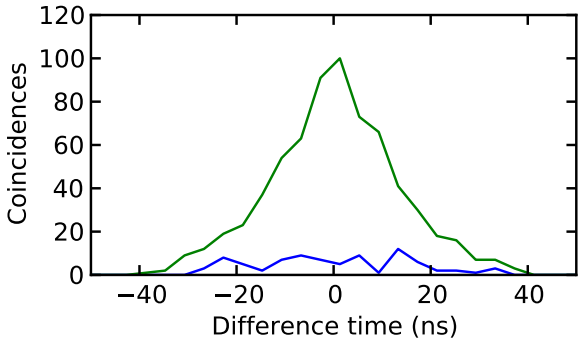

FIG. S6. Two-photon quantum interference between indistinguishable single photons leads to bunching at the output of a beam splitter This is reflected in a suppressed probability of detecting coincident clicks at each APD during the same entanglement generation element (blue). This interference is not present for events in which one APD clicks during one entanglement generation element, while the other APD clicks during the next entanglement generation element (green).

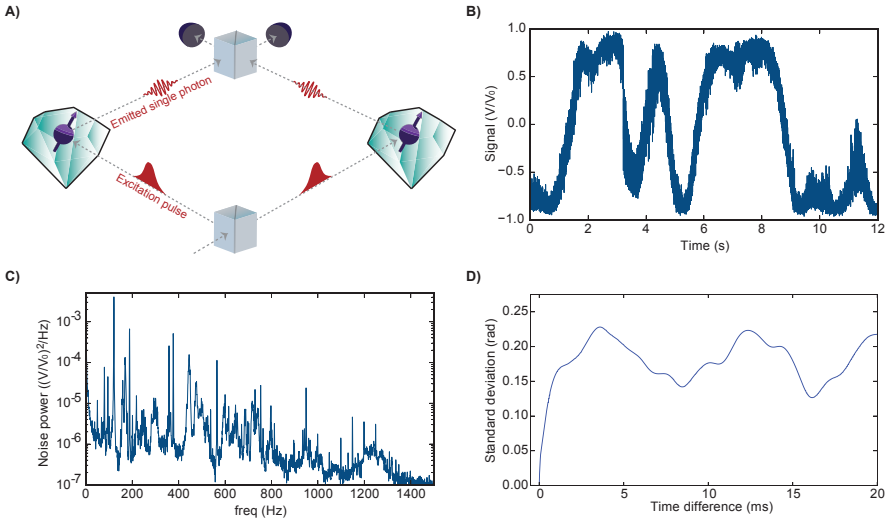

FIG. S7. a) The entanglement protocol imprints a phase on the entangled state that depends on the relative phase of the excitation laser pulses, as well as the difference in the phase acquired by the single photons as they propagate from the NVs to a central beam splitter This creates an effective interferometer, starting where the excitation pulses are separated at an initial beam splitter, and ending at the final beam splitter b) Classical light traversing the interferometer, but reflecting off of the NV sample instead of exciting the NV, is subject to the same phase fluctuations as the entangled states. This allows us to easily probe the expected phase stability of the protocol. Here classical light is inserted into the interferometer, and the output intensity is measured at one output port of the final beam splitter using a photodiode. Fluctuations in the output intensity over time are seen due to changes in the relative path length. c) Noise spectral density of the interferometer output showing many several sharp resonances below 1 kHz. d) Standard deviation of the inferred phase difference between sets of sample points separated by a fixed time difference. As can be seen, a phase difference is rapidly acquired within about 1 ms, but then the dynamics are dominated by a few resonant frequencies that periodically increase and then decrease the phase difference.

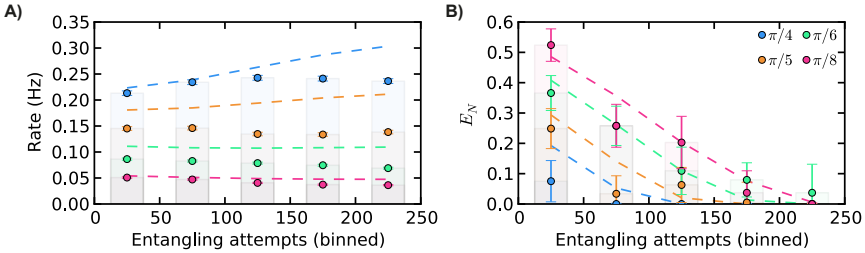

FIG. S8. a) The corresponding estimated protocol success rate (error bars are smaller than the points). Also shown in both plots are the predictions of our model (dashed lines). We partially attribute the deviation of the model to ionization of the NV electron spin while trying to generate entanglement. b) The experimentally estimated distillable entanglement E_N of the distilled state as a function of θ and elapsed second round entanglement generation attempts.

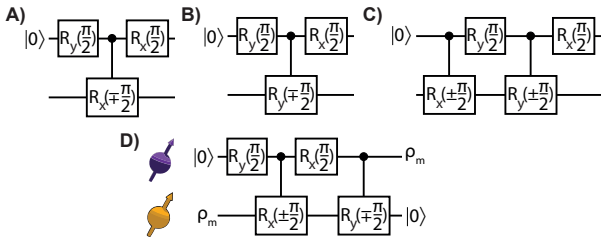

FIG. S9. Panels A-C) Read-out sequences of the nuclear spin expectation values $\hat{X}$, $\hat{Y}$, $\hat{Z}$ *(26)*. All gate circuits are followed by a single-shot measurement of the electron spin. Panel D) Nuclear spin initialization sequence. $\rho_{\mathrm{m}} = \mathbb{I}/2$ is the mixed state.

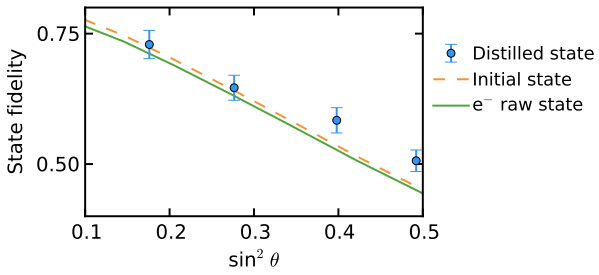

FIG. S10. Distilled state fidelities (blue) and communication qubit raw state fidelities (green) reproduced from Fig. 4B of the main text. Also shown is the best-case fidelity of the raw state if the optical phase was perfectly known at all points of the protocol (dashed orange).

	Node A	Node B	Description
$A_{\parallel}$ (kHz)	$-2\pi \cdot 30(1)$	$2\pi \cdot 33(1)$	Parallel hyperfine coupling with electron spin.
$A_{\perp}$ (kHz)	$2\pi \cdot 88(1)$	$2\pi \cdot 35(1)$	Perpendicular hyperfine coupling with electron spin.
N	12	34	Number of inversion pulses on electron for nuclear spin gate.
τ (μs)	21.772	12.812	Optimized interpulse delay for nuclear spin gate.
F_{tomo}	0.973(3)	0.978(2)	Correction factor for gate errors in the tomography sequence.
$T^*_{2,0}$ (ms)	3.4(1)	19.4(3)	Nuclear dephasing time with the electron idle in $\|m_s = 0\rangle$.
$T^*_{2,1}$ (ms)	3.4(1)	16.2(3)	Nuclear dephasing time with the electron idle in $\|m_s = \pm 1\rangle$.
σ	273(5)	272(4)	fitted $1/e$ value of the memory decay in entangling attempts.

TABLE S1. Measured experimental parameters of the nuclear spins.

Term	Description
CR check	charge-resonance check *(45)*.
Success?	ADwin verifies whether a condition of success is fulfilled or not.
wait: suc high	ADwin waits until success is signaled by the other ADwin.
not / suc	ADwin-ADwin communication via a three-way handshake.
wait for done	ADwin waits for the AWG signaling the end of a subsequence.
SSRO	single-shot readout of the NV electron spin *(31, 45)*.
Trigger	Signals the AWG to start with the sequence.
Fail/done after nth trial	AWG signals the respective ADwin the end of entangle 1 or 2.
Jump	Event jump channel of the AWG that induces a jump to the next subsequence.
^{13}C init	Initialization of the memory into the state $\|0\rangle$.
entangle 1 and entangle 2	Generate long-distance entanglement.
Count	ADwin counts the number of repetitions of a specific sequence element.
wait for jump	AWG waits for a jump command from the ADwin. If no jump (e.g. signifying a failed SWAP on one of both sides) is sent within the prespecified waiting time we return to the beginning of the sequence.
SWAP	Subsequence to swap the NV state onto the memory.
Phase	Nuclear phase feedback via dynamical decoupling of the electron spin.
calculate reps	ADwin calculates the number of dynamical decoupling cycles to obtain the desired memory phase.
Purifying gate	Step 4 of the experimental protocol (see Fig. 1 of the main text).
wait for SSRO	AWG waits until ADwins have obtained a SSRO result.
-1 : Jump	Go to a phase-adjusted tomography sequence if communication qubit was measured in $\|1\rangle$.
Tomography	One of the gate sequences depicted in Fig. S9.

TABLE S2. Glossary for all terms and abbreviations contained in Fig. S2.

Param.	Value	Description
V	0.72	Indistinguishability between photons produced by the two NVs (Section H).
p_{s}	0.01	Failure probability for classical spin-photon correlations *(28)*.
p_{d1}	$8 \cdot 10^{-4}$	Single-photon detection probability after the central beam splitter, given that NV_1 is in $\|0\rangle$.
p_{d2}	$4 \cdot 10^{-4}$	Single-photon detection probability after the central beam splitter, given that NV_2 is in $\|0\rangle$.
p_{dc}	$2.5 \cdot 10^{-6}$	Dark count probability within detection window.
p_{gate}	0.0163	Error rate for electron-nuclear-spin two-qubit gates.
p_{proj}	0.985	Probability that the NV is left in $\|m_s = 0\rangle$, given the corresponding SSRO measurement result.
ϕ		First entangled state phase. The ideal protocol is insensitive to this parameter.
$\Delta\phi$	Section I	Difference in phase between the two entangled states.
p_{m}	Sections A & G 2	Memory dephasing probability during the interval between the generation of the two entangled states.

TABLE S3. Measured experimental parameters used in our error model.

$\sin^2(\theta)$	P-value comm. qubit state	P-value phase-stable state
$\pi/8$	0.26	0.41
$\pi/6$	0.26	0.41
$\pi/5$	0.0095	0.023
$\pi/4$	0.0032	0.0086

TABLE S4. P-values for the null hypothesis that the final state fidelity is not increased from the highest-fidelity raw state.